Preprints.org

Article

Not peer-reviewed version

The Phenology of the Main Central European Host Plants (*Urtica dioica* and *Convolvulus arvensis*) of the Grapevine Pathogen Vector *Hyalesthes obsoletus* and Their Potential Relevance for Predicting the Onset of the Vector's Flight

Helmut Gangl , Gerhard Leitner , Martin Tiefenbrunner , Wolfgang Tiefenbrunner *

Posted Date: 6 November 2025

doi: 10.20944/preprints202510.2130.v1

Keywords: *Hyalesthes obsoletus*; *Urtica dioica*; *Convolvulus arvensis*; Bois noir; phenology; prediction model

Preprints.org is a free multidisciplinary platform providing preprint service that is dedicated to making early versions of research outputs permanently available and citable. Preprints posted at Preprints.org appear in Web of Science, Crossref, Google Scholar, Scilit, Europe PMC.

Copyright: This open access article is published under a Creative Commons CC BY 4.0 license, which permit the free download, distribution, and reuse, provided that the author and preprint are cited in any reuse.

Preprints.org (www.preprints.org) | NOT PEER-REVIEWED | Posted: 6 November 2025 doi:10.20944/preprints202510.2130.v1

Disclaimer/Publisher's Note: The statements, opinions, and data contained in all publications are solely those of the individual author(s) and contributor(s) and not of MDPI and/or the editor(s). MDPI and/or the editor(s) disclaim responsibility for any injury to people or property resulting from any ideas, methods, instructions, or products referred to in the content.

Article

The Phenology of the Main Central European Host Plants (*Urtica dioica* and *Convolvulus arvensis*) of the Grapevine Pathogen Vector *Hyalesthes obsoletus* and Their Potential Relevance for Predicting the Onset of the Vector's Flight

Helmut Gangl [1], Gerhard Leitner [1], Martin Tiefenbrunner [2] and Wolfgang Tiefenbrunner [1,*]

[1] Federal Office of Viticulture, 7000 Eisenstadt, Gölbesstraße 1, Austria

[2] Logistic Management Service, Rosenstraße 7, 80331 Munich, Germany

* Correspondence: w.tiefenbrunner@bawb.at

Abstract

Hyalesthes obsoletus is the most efficient vector of the causal agent of Bois noir disease in grapevine. For the purpose of integrated disease management, models based on temperature sums have been developed to predict the onset of adult flight of this vector. However, the predictive accuracy of these models varies locally. It was demonstrated that the timing of adult emergence in the 17-year cicada *Magicicada* sp., which—like *H. obsoletus*—develops underground, is determined by the number of host plant seasons experienced and thus its phenology. If a similar relationship exists between the larval development of *H. obsoletus* and the phenology of its preferred host plants (*Urtica dioica* and *Convolvulus arvensis*), then the predictive accuracy of existing models might be improved by incorporating host-phenology data. In the present study, we first examined how soil-dwelling organisms that lack access to photoperiodic cues might nonetheless perceive day length (and thereby seasonal timing and periodicity). Simulations and analyses of soil temperature sensor data from the study area showed that, at a depth of 20 cm, the temperature amplitude amounts to only about 9–17 % of that at the soil surface—probably insufficient on some days to allow determination of day length. It is therefore plausible, though not proven, that host-physiological processes related to phenology influence larval development of *H. obsoletus*. Host plant phenology was monitored over three years and compared with model predictions of *H. obsoletus* flight onset. The vegetative development of *U. dioica* and *C. arvensis* did not yield parameters capable of improving the predictive models. Parameters assessed included stem or shoot length, number of internodes and leaves, and leaf area. More promising were traits associated with generative development—particularly the number of nodes with inflorescences per stem in *U. dioica* and the onset of flowering in *C. arvensis*.

Keywords: *Hyalesthes obsoletus*; *Urtica dioica*; *Convolvulus arvensis*; Bois noir; phenology; prediction model

Introduction

The Palaearctic bindweed planthopper *Hyalesthes obsoletus* Signoret (Hemiptera: Cixiidae) is the most efficient known vector of the phytopathogenic bacterium *"Candidatus Phytoplasma solani"* (class *Mollicutes*, order *Acholeplasmatales*, taxonomic subgroup 16SrXII-A), the causal agent of grapevine Bois noir disease (Quaglino et al., 2013). The adult insects are polyphagous and are therefore capable of transmitting the pathogen from the host species on whose roots the larvae feed to a broad range of cultivated and wild plants—over 90 species across 36 families. *Ca. P. solani* can cause substantial economic losses in certain crops.

© 2025 by the author(s). Distributed under a Creative Commons CC BY license.

Preprints.org (www.preprints.org) | NOT PEER-REVIEWED | Posted: 6 November 2025 doi:10.20944/preprints202510.2130.v1

The vector *H. obsoletus* feeds on the phloem of its host plants using specialised piercing–sucking mouthparts and can infect them in the process. Infection appears to occur readily, for example as a side effect of probing plants for host suitability. This thermophilous species is distributed throughout the Mediterranean region, extending northwards and eastwards to Germany and Russia. It is commonly found on sunny slopes and roadsides (Panassiti et al., 2013). As an adult, *H. obsoletus* lives for a maximum of six weeks, during June and July. Females deposit their eggs in the soil close to the roots of the local larval host plants. The larvae, which are soil-dwelling and root-feeding, pass through five developmental instars (described in detail by Sforza et al. 1999 and Tiefenbrunner & Tiefenbrunner 2025). Across its distribution range, 25 overwintering hosts have so far been identified. Because the larvae are restricted to a limited number of reproductive host plants, they are unable to acquire phytoplasmas from cultivated plants or to transmit them to such crops. Consequently, in epidemic cycles involving *H. obsoletus* as the pathogen vector, cultivated plants always act as terminal hosts (Johannesen et al., 2008; Jović et al., 2019).

In western and central Europe, the stinging nettle *Urtica dioica* and the field bindweed *Convolvulus arvensis* are of particular epidemiological importance for *Ca. P. solani*, as they almost invariably serve as the source of the phytoplasma infections (Langer & Maixner, 2004; Aryan et al., 2014; Landi et al., 2015). Sequence analyses of the elongation factor Tu (tuf) gene in *Ca. P. solani* isolates have identified two main lineages, tuf-a and tuf-b, associated with *U. dioica* and *C. arvensis*, respectively. Accordingly, there exist two independent epidemic cycles linked to these hosts (Langer & Maixner, 2004; Riedle-Bauer et al., 2013). Studies in Austria further revealed an intermediate genealogical lineage between tuf-a and tuf-b, designated tuf-b2, which is associated with *U. dioica* (Aryan et al., 2014).

As early as 1981, Imo concluded from genetic investigations that *H. obsoletus* had also developed host-specific races. This has since been confirmed by genetic analyses employing random amplification of polymorphic DNA (RAPD) and simple sequence repeat (SSR) markers (Johannesen et al., 2008; Imo et al., 2013).

In addition to the pathogen and its principal vector, the main host plants themselves are crucial components of the epidemic cycles. However, they have received comparatively little scientific attention (but note Šrůtek & Teckelmann, 1998; Paulauskienė, 2021), despite indications that their phenology may strongly influence the larval development of *H. obsoletus*. A comparison illustrates this possibility: in a study on the timing of adult emergence in the 17-year cicada *Magicicada* sp., Karban et al. (2000) demonstrated that this species determines its pre-adult developmental period—which, as in *H. obsoletus*, takes place underground—not by accumulating temperature degree-days or measuring elapsed time, but by counting the number of host plant seasons (as Alexander and Moore had already postulated in 1962). By artificially altering the thermo-photoperiod, the authors induced their host trees to flower and shed leaves twice within a single year; as a result, adult emergence occurred after only 16 years instead of 17. They therefore inferred that the cicadas respond to host phenology, which they may perceive through seasonal fluctuations in xylem flow.

Animals whose larval development takes place in the soil cannot be directly influenced by photoperiod and therefore cannot rely on it as an external time cue. The amplitude of annual and, in particular, daily thermal cycles diminishes progressively with increasing soil depth relative to the temperature at the air–soil interface. This applies equally to the developmental stages of *H. obsoletus* and *Magicicada* sp., making it plausible that both have evolved comparable strategies to compensate. In the phloem, for example, developmental processes such as inflorescence formation or nectar production may affect sugar flow to the roots. The phloem also transports phytohormones (including cytokinins and gibberellins, which are relevant for flower development, as well as abscisic acid, brassinosteroids, and certain auxins) downstream to the roots. These may be perceived by the larvae and could contribute to synchronising larval development and the timing of adult emergence.

A direct demonstration of a causal link between host and vector phenology in *H. obsoletus*—analogous to *Magicicada* sp.—could be achieved by artificially altering photoperiod and thus the developmental rhythm of the host plant while maintaining constant soil temperature.

© 2025 by the author(s). Distributed under a Creative Commons CC BY license.

Preprints.org (www.preprints.org) | NOT PEER-REVIEWED | Posted: 6 November 2025 doi:10.20944/preprints202510.2130.v1

Within the limits of our research facilities, we set more modest objectives. First, we examined how the amplitude of daily thermal cycles decreases with soil depth, in order to determine whether such temperature oscillations could be perceived as indicators of elapsed days or, more specifically, of day length. Furthermore, we recorded the phenology of the host plants over a period of three years at several sites and compared these data with predictions from a temperature-sum-based model (Maixner & Langer, 2006; Maixner & Johannesen, 2014) that forecasts the timing of adult emergence in *H. obsoletus*. This model provides excellent agreement with observations in our study area (eastern Austria), though less so in certain other regions. Combining the model with host-phenology data could potentially improve its predictive accuracy for flight onset and thereby for the seasonal dynamics of pathogen spread, enabling its application across a wider geographical range. The model is currently employed in the integrated management of Bois noir disease.

Methods

- **Description of sampling sites for host plants**

Convolvulus arvensis: Five sites were selected for sampling (Figure 1), all situated either on the slopes of the Leithagebirge ("Leitha Mountains") and/or near the Neusiedlersee ("Lake Neusiedl") in proximity to vineyards. Four of these sites were located in the immediate vicinity of a weather station (Großhöflein, Donnerskirchen–Wolfsbrunnbach, Winden, Gols), while one (Donnerskirchen–Goldberg) was 732 m from the nearest station. The Donnerskirchen sites were additionally situated at or near the position of soil sensors.

Urtica dioica: The nettle sampling sites were located somewhat farther from vineyards and weather stations, as *U. dioica* differs from *C. arvensis* in its habitat requirements. To compensate, a larger number of sampling sites—eight in total—were selected, all situated either along the slopes of the Leithagebirge or near the lake. Some were located directly adjacent to a water body (retention basins near Oslip, Kleinhöflein, and Hornstein), to a forested area (Hornstein, Großhöflein, Rust), or to a tree-lined embankment (Oslip, Donnerskirchen). For the prediction of *Hyalesthes obsoletus* flight onset, the weather stations closest to each sampling site were used (Figure 1).

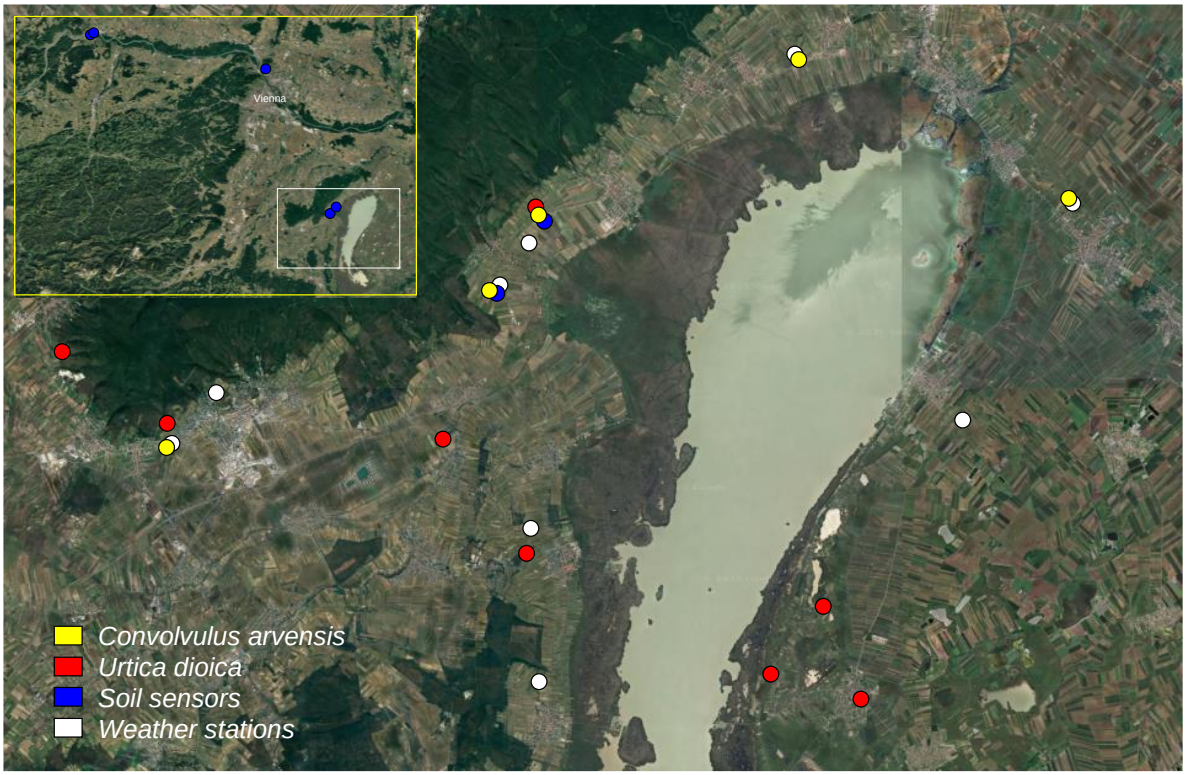

© 2025 by the author(s). Distributed under a Creative Commons CC BY license.

Preprints.org (www.preprints.org) | NOT PEER-REVIEWED | Posted: 6 November 2025 doi:10.20944/preprints202510.2130.v1

Figure 1. Sampling sites for host plants, weather stations, and soil sensors. Sites located near the Danube are shown in the inset (upper left).

Soil Sensors and Weather Stations

At the end of March 2022, temperature–soil moisture sensors (IoT-Systems, Austria) were installed at five sites in eastern Austria, positioned at soil depths of 5 cm and 20 cm. In addition, an air temperature–humidity sensor was placed at the soil surface, followed later in the year by another identical unit positioned at approximately 2 m height. The sensors recorded data every 20 minutes; however, the outputs were transmitted to the authors at two-hour intervals.

This instrumentation was deployed at two sites east of Eisenstadt (Donnerskirchen–Wolfsbrunnbach and Donnerskirchen–Goldberg), approximately 40 km southeast of Vienna, at Langenzersdorf north of Vienna, and at two sites near Krems (Krems–Sandgrube and Krems–Schule), about 60 km west of Vienna near the Danube.

- **Predictive model for the flight onset of *Hyalesthes obsoletus* (after Maixner & Johannesen 2014)**

Maixner & Langer (2006) and Maixner & Johannesen (2014) developed simple predictive models for determining the timing of adult emergence (imaginal moult) and thus the onset of flight in *H. obsoletus*. These models were used here for comparison with the phenological data of *U. dioica* and *C. arvensis* and are therefore briefly summarised below.

In these models, the onset of flight is calculated based on the required accumulated temperature sum (degree-days). Two parameters are essential:

1. the **start date**, i.e. the day from which daily mean temperatures begin to be accumulated, and
2. the **minimum threshold temperature**, which must be exceeded before the daily mean contributes to the total sum.

In addition, a specific cumulative temperature value is defined at which the onset of flight is predicted. Different parameter values are assumed for the respective host plants (Table 1).

Table 1. Parameters of the model by Maixner & Johannesen (2014) used to estimate the probable onset of *H. obsoletus* flight.

	Stinging nettle	field bindweed
Start date of summation	01. April	09. March
Temperature threshold	5°C	5,8°C
Required temperature sum	1160	1053

For model calculations, Maixner & Johannesen (2014) used air temperature data (daily means measured at 2 m above ground) from the nearest available weather station. The model has since been implemented, for example, in the VitiMeteo system developed by OTT HydroMet GmbH (Germany). Besides predicting the expected timing of adult emergence, the model also issues a recommendation to cease any control of host plants once 60 % of the required temperature sum has been reached.

For the present comparison between model predictions and host plant phenology of *H. obsoletus*, temperature data were obtained from nearby weather stations installed within or adjacent to vineyards as part of the ClimVino Interreg research project (2019–2022), which aimed to optimise plant protection product use in viticulture (Figure 1).

- **Physical Basis of Heat Diffusion in Soil**

Maixner and Johannesen (2014) used temperature data measured at a height of 2 m above ground level for their model; however, the larval stages of *Hyalesthes obsoletus* are exposed to soil temperature, which alone governs their development. In the present study, heat propagation in the soil at the sampling sites was therefore modelled, primarily to determine how daily temperature fluctuations penetrate into the ground. The physical foundation of this approach is Fourier's (1822)

© 2025 by the author(s). Distributed under a Creative Commons CC BY license.

Preprints.org (www.preprints.org) | NOT PEER-REVIEWED | Posted: 6 November 2025 doi:10.20944/preprints202510.2130.v1

heat conduction equation. Because only the vertical axis is relevant when simulating thermal diffusion in soil, this partial differential equation simplifies to:

1) $$\frac{\partial T}{\partial t} = \alpha \frac{\partial^2 T}{\partial z^2}$$ where:

- T = temperature
- t = time
- z = position (soil depth)
- α = thermal diffusivity constant

The material-specific diffusivity constant α depends on soil composition and compaction, as well as on soil moisture content, since air and water conduct heat to differing degrees. The simulation was implemented using the Delphi 7 Aurora IDE (Borland, USA) and Delphi CE (Embarcadero, USA). Model results were compared with empirical measurements obtained from soil temperature sensors.

- **Description of the Vegetative Development of the Host Plants**

From the appearance of above-ground plant parts—between late February and early March in *Urtica dioica* and from early to late April in *Convolvulus arvensis*—the following measurements were carried out: stem or shoot length, number of internodes, number of leaves, and area per leaf. The numbers of internodes and leaves may be only weakly correlated, as basal leaves are often lost due to shading and/or fungal infection. From individual leaf area and number of leaves, total leaf area per "individual" (i.e. stem or shoot) was calculated and included in the statistical analyses. It should be noted that the above-ground shoots or stems are interconnected via rhizomes and thus represent parts of a single individual. Measurements were discontinued in June, a few weeks after the onset of generative development.

Urtica dioica exhibits opposite leaf arrangement with dimers (very rarely trimers) at each node, i.e. twice as many leaves as nodes. *C. arvensis* displays alternate leaf arrangement, forming an equal number of nodes and leaves. Secondary leaves or leaves from lateral shoots were not considered.

- **Determination of Leaf Area**

All leaves were scanned against a blue background (blue being efficiently absorbed during photosynthesis and thus providing high contrast), and total leaf area was determined by counting the pixels identified as belonging to the leaf surface. Identification was based on colour ratios. Each pixel is represented by an RGB vector with intensity values for red, green, and blue ranging from 0 to 255. The values of this colour cube were scaled to the range 0–1 according to equation (2):

(2) Red′ + Green′ + Blue′ = 1

This condition can be fulfilled through the following transformations:

Red′ = Red / (Red + Green + Blue)

Green′ = Green / (Red + Green + Blue)

Blue′ = Blue / (Red + Green + Blue)

It is straightforward to verify that substituting these transformed values into equation (2) satisfies the condition. All points fulfilling this equation lie on the **unit simplex** (Figure 2)—a plane within the RGB cube defined by the vertices RGB(1,0,0), RGB(0,1,0), and RGB(0,0,1). All possible colour ratios form an equilateral triangle, which subsequently serves as the operational basis. The surface of the simplex was rasterised, and those cells corresponding to RGB ratios characteristic of leaf colours were selected (yellow region in Figure 2, right triangle).

The accuracy of leaf-pixel recognition was verified by colouring the identified pixels yellow on the scanned leaf image (Figure 2, lower right). Across the three study years, a total of 13,482 *U. dioica* leaves and 5,764 *C. arvensis* leaves were measured.

© 2025 by the author(s). Distributed under a Creative Commons CC BY license.

Preprints.org (www.preprints.org) | NOT PEER-REVIEWED | Posted: 6 November 2025 doi:10.20944/preprints202510.2130.v1

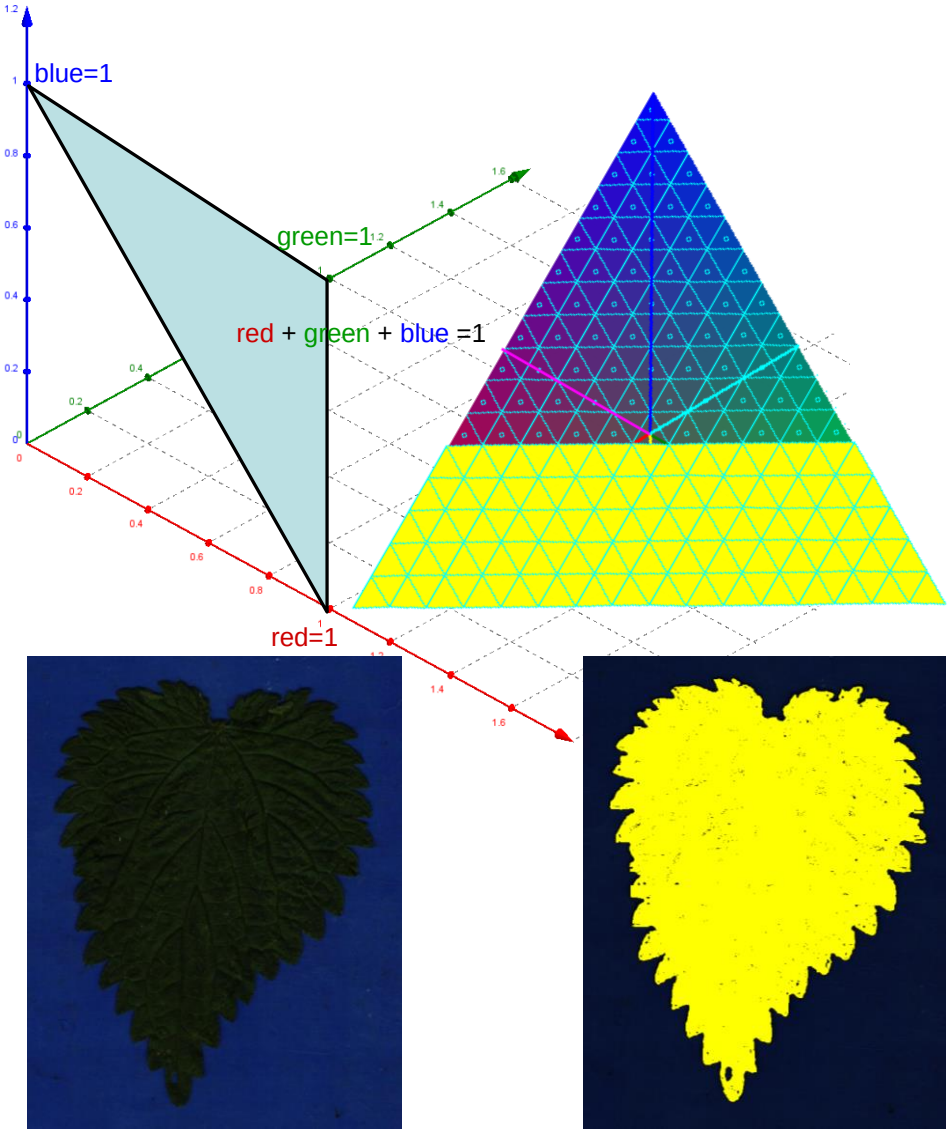

Figure 2. Representation of the unit simplex satisfying equation (2). All pixel colour values are transformed so that they lie on the simplex, ensuring that differences in brightness caused by variable illumination do not affect detection. The simplex serves to identify those pixels belonging to the leaf surface. Further explanation is provided in the text.

- **Description of the Generative Development of the Host Plants**

Urtica dioica: From late May to early June, inflorescences of *U. dioica* appear at the distal nodes, with floral primordia being less developed the closer they are to the shoot apex. *U. dioica* is generally dioecious. For the assessment of developmental stages, the second-lowest inflorescences on each shoot were selected. Floral development was divided into discrete stages as follows (Figure 3):

Female flowers (lens- to lanceolate-shaped):

Stage	Description
0	"Hedgehog stage": perianth green, stinging hairs on the floral apex still distinct.
1	Flower closed, perianth green, few or no stinging hairs; apex with (more or less) long reddish remnants; noticeably larger than in the previous stage.

© 2025 by the author(s). Distributed under a Creative Commons CC BY license.

Preprints.org (www.preprints.org) | NOT PEER-REVIEWED | Posted: 6 November 2025 doi:10.20944/preprints202510.2130.v1

Stage	Description
2	Flower closed except at the distal tip; no stinging hairs or reddish remnants; visibly larger than in stage 1.
3	Flowers open, ovary visible, perianth often slightly reddish.
4	Withered: ovary visible, perianth wilted.

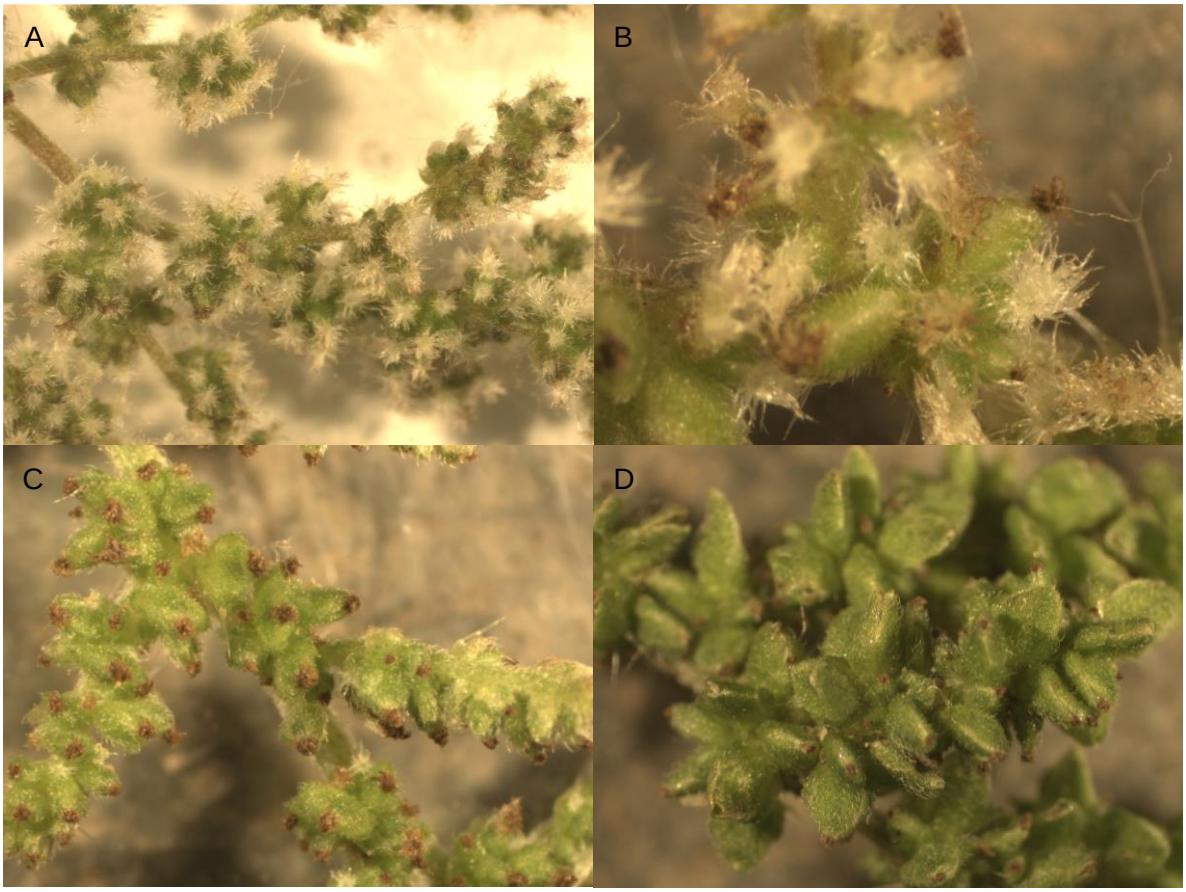

Figure 3. Female flowers of *U. dioica*: A – flowers at stage 0 ("hedgehog stage"); B – flowers at stages 0–1; C – flowers at stage 1;D – flowers predominantly at stage 2, some already at stage 3.

Male flowers (rounded):

Stage	Description
1	Closed; perianth green, stinging hairs still distinct.
2	Closed; perianth often reddish, few stinging hairs.
3	Closed except at the distal end; perianth margins whitish to light green (anthers visible through); flower volume distinctly larger than in previous stage.
4	Open, but stamens not yet extended.
5	Open, stamens fully extended.
6	Withered, possibly abscised.
7	Inflorescence completely desiccated.

© 2025 by the author(s). Distributed under a Creative Commons CC BY license.

Preprints.org (www.preprints.org) | NOT PEER-REVIEWED | Posted: 6 November 2025 doi:10.20944/preprints202510.2130.v1

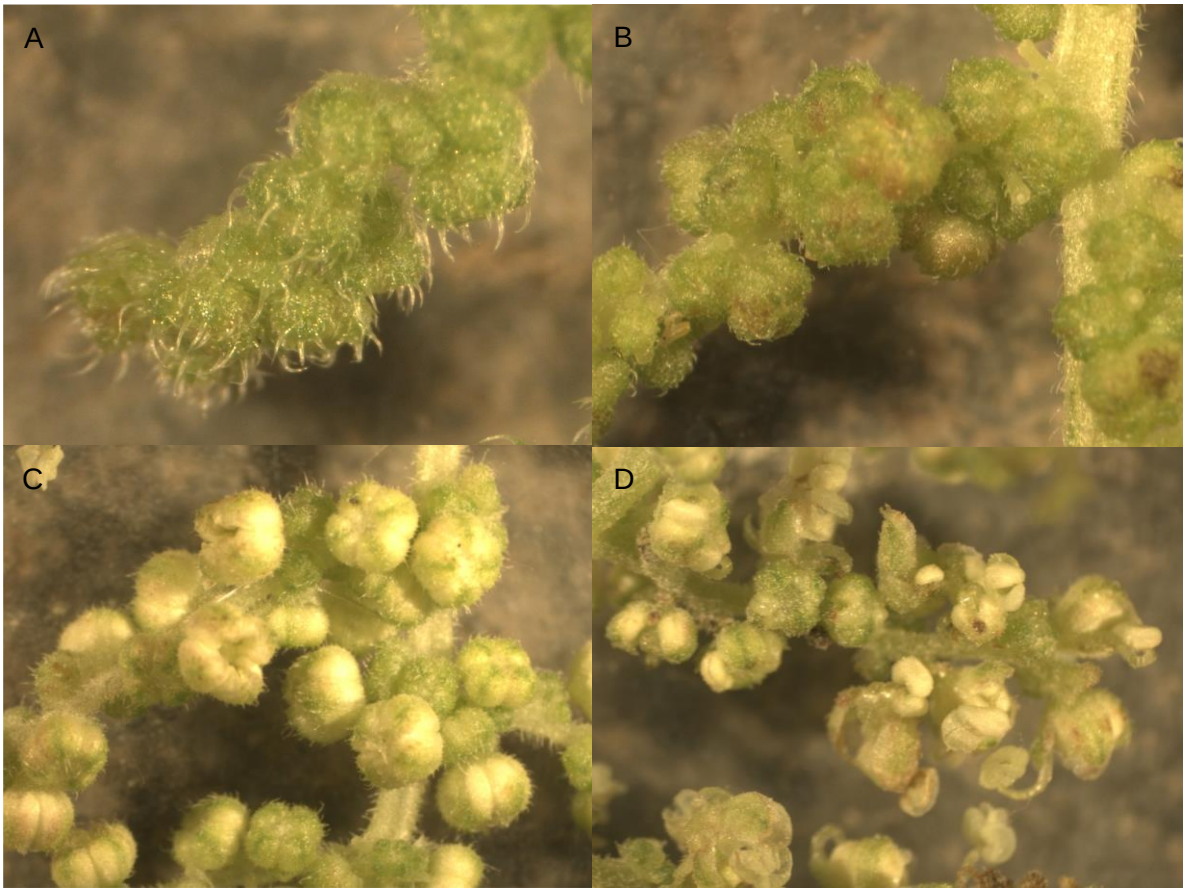

Figure 4. Male flowers of *U. dioica*: A – stage 1; B – predominantly stage 2; C – stage 3; D – stages 4 and 5.

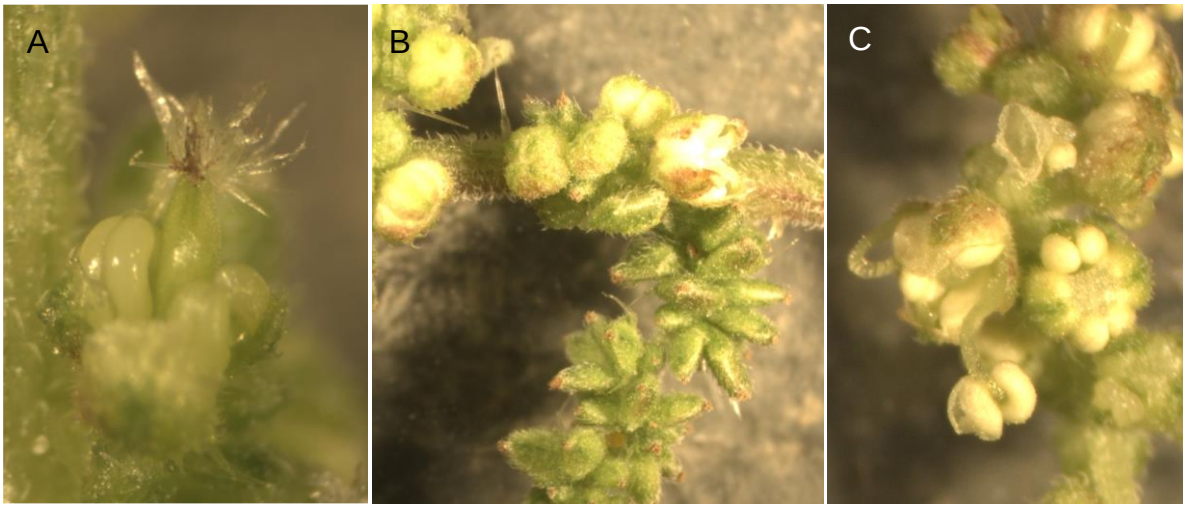

Figure 5. *U. dioica*: A – rare hermaphroditic flower; B – inflorescence bearing both male and female flowers; C – purely male flowers (for comparison with A).

Inflorescences at a given node may be either entirely male or entirely female, yet both sexes can occur on the same individual. In most cases, *U. dioica* is dioecious.

The relative frequency of each stage per inflorescence was recorded, and the median developmental stage was determined on the basis of rank values. In addition, the number of nodes bearing inflorescences per individual was recorded.

Convolvulus arvensis: For each "individual", the numbers of generative buds, as well as of closed, open, and withered flowers, were determined. Proximal flowers are older and therefore generally more advanced in development than distal ones.

© 2025 by the author(s). Distributed under a Creative Commons CC BY license.

Preprints.org (www.preprints.org) | NOT PEER-REVIEWED | Posted: 6 November 2025 doi:10.20944/preprints202510.2130.v1

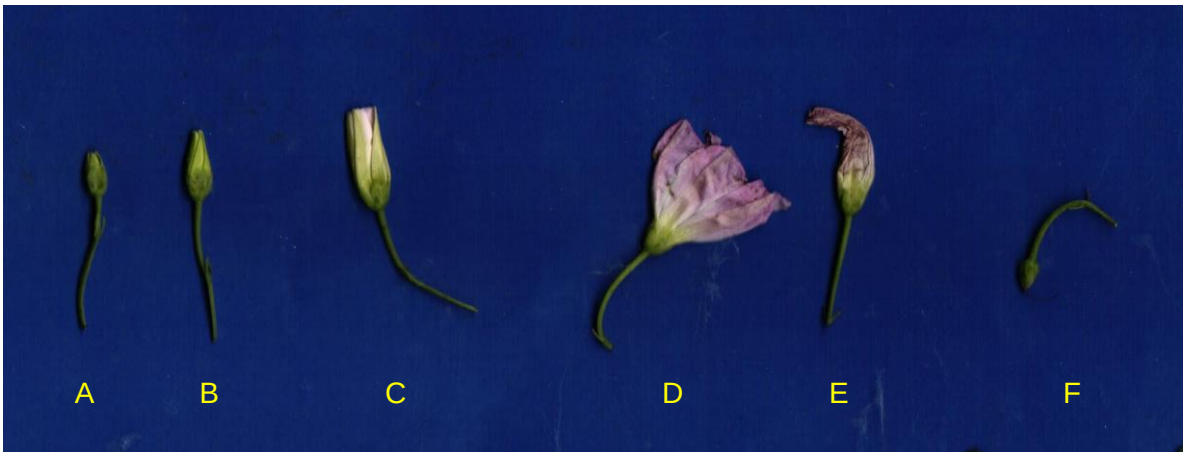

Figure 6. Monoecious flowers and flower stages of *C. arvensis*: A, B – flower buds; C – closed flower; D – open flower; E – withered flower; F – ovary (petals and stigma lost).

- **Statistics:**

The statistical analyses (mainly regressions) were performed using Statgraphics Centurion Version XV (Statgraphics Technologies, Inc.,The Plains, Virginia).

Results

- **Heat Diffusion from the Soil Surface into Depth**

Within the framework of this study, the propagation of heat in the soil was investigated and modelled at the selected sites. A key aspect was the determination of the site-specific diffusion constant, α_{site}, as a function of current soil moisture.

There is a simple observation which leads to a crucial insight: Figure 7 shows temperature courses in the air (0 cm, 200 cm) and in the soil (–5 cm, –20 cm) over nine consecutive days (Langenzersdorf, mid-May 2022). The daily temperature fluctuations are clearly dampened and phase-shifted as they penetrate into the soil. The diurnal amplitude is most pronounced at ground level (air at 0 cm), reaching a maximum of more than 43 °C in the observation interval (early afternoon), whereas nocturnal values differ little from those at 2 m height—thus reflecting primarily the effect of solar radiation on the soil surface (for which no sensors were available). At 5 cm depth, the amplitude is already markedly reduced (exceeding 30 °C only once), and the temperature maximum is reached with a delay of approximately one hour.

© 2025 by the author(s). Distributed under a Creative Commons CC BY license.

Preprints.org (www.preprints.org) | NOT PEER-REVIEWED | Posted: 6 November 2025 doi:10.20944/preprints202510.2130.v1

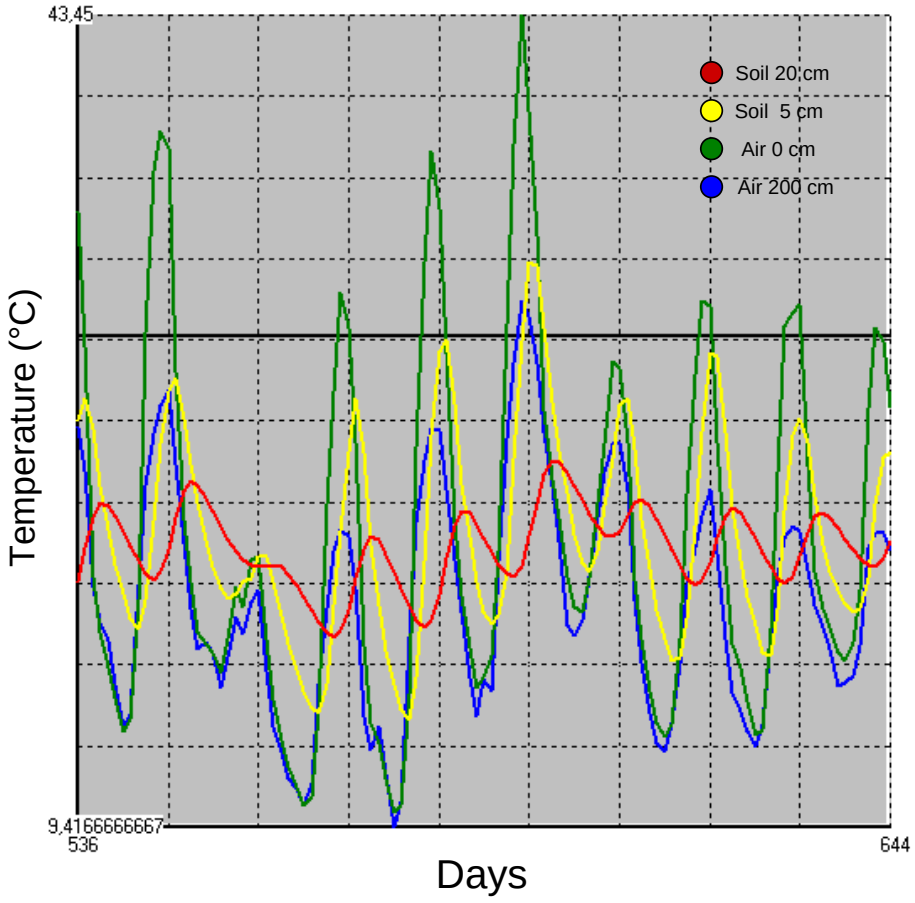

Figure 7. Output of temperature sensors (heights: 200 cm, 0 cm, –5 cm, –20 cm) during a nine-day interval in mid-May 2022 at the Langenzersdorf site. A decrease in amplitude and a phase lag with increasing soil depth are clearly visible over the diurnal cycle. At 20 cm depth, the amplitude is even less pronounced, and the maximum occurs only after about six hours.

Using an analytical reference model, this information can be employed to determine the local diffusion constant. For this purpose, a software tool was developed that discretises the diffusion process in both spatial and temporal dimensions. For the example shown in Figure 8, it was assumed that the surface temperature varies sinusoidally over the course of the day. The soil profile was divided into horizontal layers of 5 cm, and at a depth of one metre a constant, low temperature was assumed. Model updates occurred every four virtual minutes, and the diffusion process was observed over several virtual days (although the simulation itself required only a few seconds of computation time).

© 2025 by the author(s). Distributed under a Creative Commons CC BY license.

Preprints.org (www.preprints.org) | NOT PEER-REVIEWED | Posted: 6 November 2025 doi:10.20944/preprints202510.2130.v1

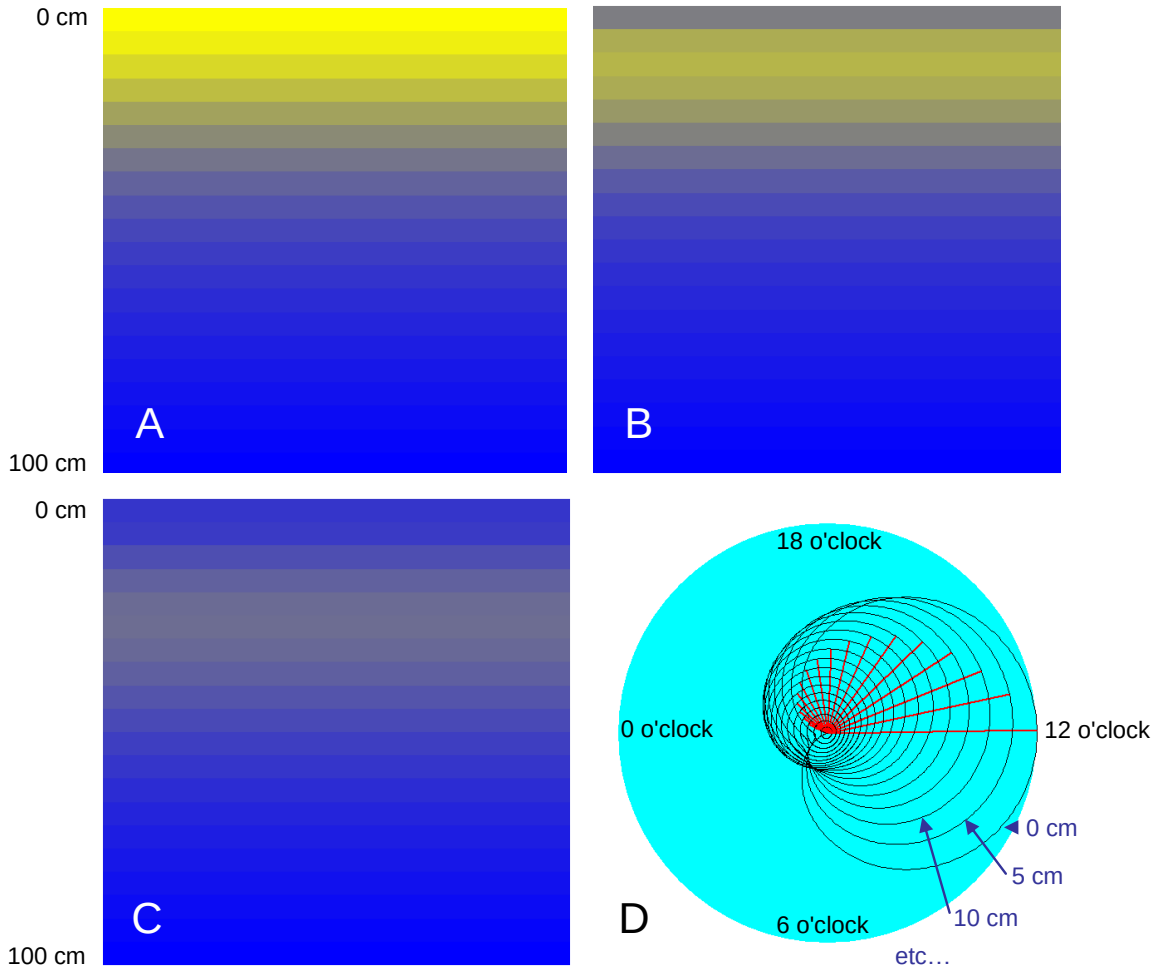

Figure 8. Simulation of heat diffusion through soil layers of increasing depth across three consecutive time steps (A–C). Panel D illustrates the corresponding decrease in amplitude (represented by the brightness of the yellow bands in A–C) and the phase shift with increasing depth. A diffusion constant of $\alpha = 0.5$ was used.

In Figure 8, the diffusion process proceeds from A to C, with $\alpha = 0.5$. The thermal wave (yellow) can be seen propagating into the soil and remaining discernible even at midnight (0 o'clock) at a depth of 25 cm, contrasting with the cooler (blue) background. Figure 8D depicts how both amplitude and phase change progressively with increasing depth. The temperature maximum is thus reached at different times depending on soil depth, with both phase shift and amplitude attenuation depending on the value of α.

To estimate α_{site}, the empirical data were compared with the model. As an example, Figure 9 shows a nine-day period (late May 2022) characterised by low soil moisture at 20 cm depth, recorded at the Langenzersdorf site. The temperature peaks are temporally shifted relative to one another (Figure 9A), indicating that heat requires a finite time to penetrate the soil. To determine this delay, two analytical tools were developed. The first allows the data of one sensor to be shifted relative to those of another.

© 2025 by the author(s). Distributed under a Creative Commons CC BY license.

Preprints.org (www.preprints.org) | NOT PEER-REVIEWED | Posted: 6 November 2025 doi:10.20944/preprints202510.2130.v1

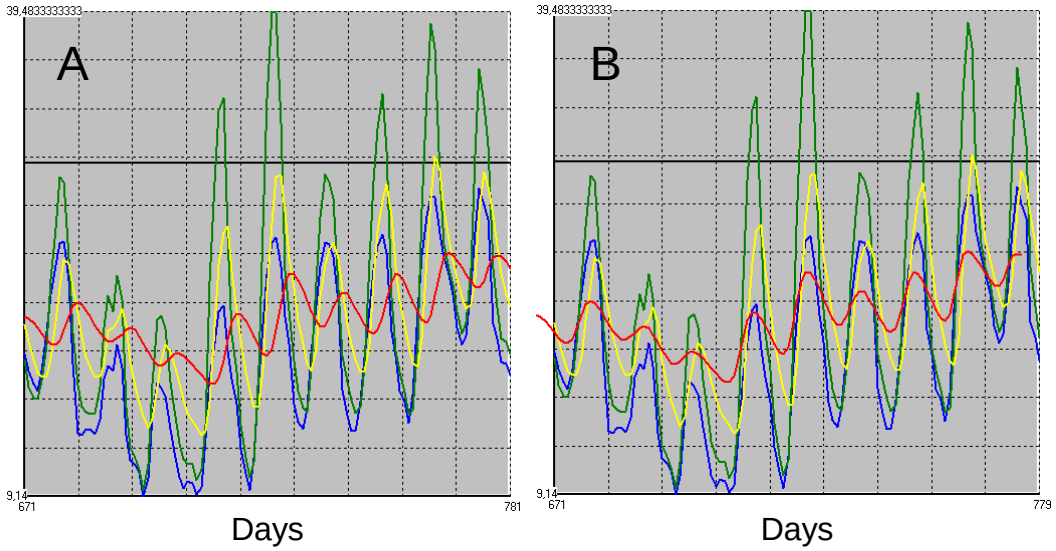

Figure 9. Temperature courses during nine days in late May 2022 at the Langenzersdorf site at different sensor depths (for colour codes see Figure 7). In B, the red curve (temperature at 20 cm depth) has been shifted relative to the green curve (air temperature at the soil surface) so that their peaks align as closely as possible.

In Figure 9B, the red curve (20 cm depth) was shifted backwards in time until its daily peaks aligned best with those of the green curve (ground-level air temperature). In this example, the heat required approximately **eight hours** to reach a depth of 20 cm.

The second tool automates the detection of the phase shift. In this procedure, a sinusoidal oscillation with a period of one day is compared with one of the temperature curves, and the **Pearson correlation coefficient** is calculated. Prior to this, both the sinusoid and the temperature curve are scaled to a common daily minimum (0) and maximum (1). The process is then repeated, shifting the sinusoid by half-hour increments until a full period has been covered, yielding 48 correlation coefficients per temperature curve. The same procedure is applied to all temperature datasets. The result is shown in Figure 10. Negative correlation coefficients appear in the inner circle; coloured lines represent the time of maximum correlation. In the present case, the phase difference between the maximum correlation of air temperature at ground level (green) and soil temperature at 20 cm depth (red) was approximately **eight hours**. This method achieves a temporal resolution of about 30 minutes, despite the fact that the raw data were available only at two-hour intervals.

© 2025 by the author(s). Distributed under a Creative Commons CC BY license.

Preprints.org (www.preprints.org) | NOT PEER-REVIEWED | Posted: 6 November 2025 doi:10.20944/preprints202510.2130.v1

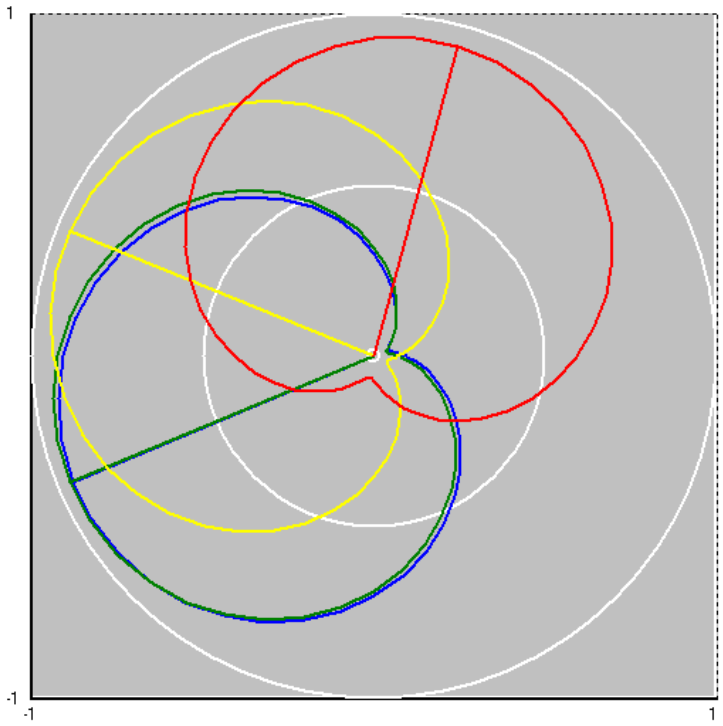

Figure 10. Phase shift and propagation velocity of the thermal wave during its passage from the surface into the soil (late May 2022, Langenzersdorf site). For colour codes see Figure 7.

The results of the analyses for all sites are summarised in Table 2. The sample size corresponds to the number of evaluable weeks (i.e. those without data loss or sensor malfunction) between April and October. The mean phase difference is given in hours. Likewise, the amplitude ratio represents an average value. The temperature amplitude denotes the difference between the daily maximum and minimum temperatures. The amplitude at 20 cm soil depth is compared with that at the surface.

Table 2. Temperature phase difference (hours) and amplitude ratio between the soil surface and 20 cm soil depth during the period April–October 2022 at all study sites (DonG = Donnerskirchen–Goldberg; DonW = Donnerskirchen–Wolfsbrunnbach; Lang = Langenzersdorf; KrSc = Krems–Schule; KrSG = Krems–Sandgrube).

site	sample size	phase difference 0 cm & -20 cm	amplitude -20 cm / amplitude 0 cm
DonG	13	8,154	0,089
DonW	14	7,464	0,095
Lang	34	8,544	0,150
KrSc	29	6,190	0,162
KrSG	24	6,250	0,165

At the Krems sites, the thermal wave required just over six hours to traverse the upper 20 cm of soil, whereas at the remaining sites the corresponding duration was roughly eight hours. Diurnal temperature fluctuations decrease progressively with depth, so that all amplitude ratios (–20 cm / 0 cm) are less than one. These ratios, however, differ among sites and are particularly low at Donnerskirchen—less than one-tenth of the surface amplitude is retained. It therefore appears doubtful whether *H. obsoletus* larvae, which may indeed occur at this depth, could utilise diurnal periodicity as a reliable temporal cue.

At Donnerskirchen–Goldberg (DonG), the soil type is a calcareous-free loose sediment brown earth, whereas at Donnerskirchen–Wolfsbrunnbach (DonW) it is a calcareous humid black earth (eBOD: https://bodenkarte.at/).

© 2025 by the author(s). Distributed under a Creative Commons CC BY license.

Preprints.org (www.preprints.org) | NOT PEER-REVIEWED | Posted: 6 November 2025 doi:10.20944/preprints202510.2130.v1

In general, a negative correlation exists between phase difference and amplitude ratio—a relationship predicted by the theoretical model. Soil moisture did not have a statistically significant effect on α_{site} during the observation period.

- **Relationship between Air Temperature at 200 cm Height and Soil Temperature at 20 cm Depth**

In the model proposed by **Maixner and Johannesen (2014)**, temperature data are taken from nearby weather stations whose sensors are positioned at a height of 2 m. For the larvae of *H. obsoletus*, however, temperatures between 5 cm and 20 cm soil depth are far more relevant. It is therefore reasonable to investigate the correlation between air and soil temperature (Figure 11) in order to assess how representative air temperature sums may be for the development of *H. obsoletus*. This relationship was examined for all study sites.

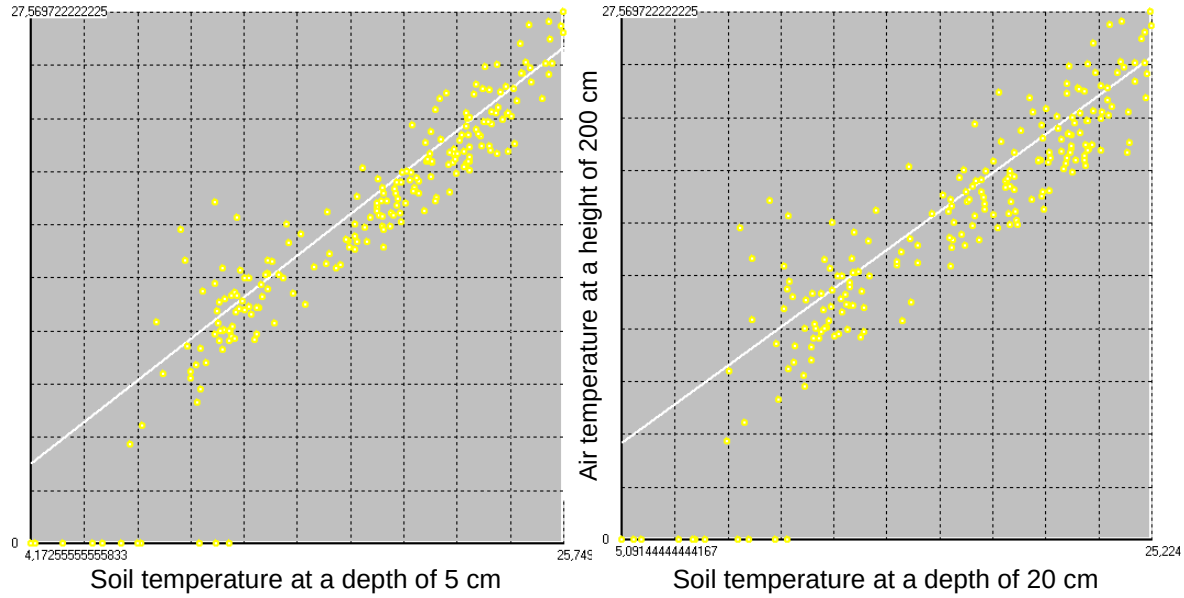

Figure 11. Relationship between soil and air temperature. The white line is not a regression line but the first median, where both axes have equal values. Since the air-temperature sensor was installed at a later stage, some values lie along the x-axis and are not relevant.

Figure 11 illustrates the results for one of the Krems sites. Comparing soil temperature (depth: 5 cm and 20 cm) with air temperature (height: 200 cm) reveals a consistently strong correlation. At the site Krems–Schule, correlation coefficients were **R = 0.99** (for comparison with the 5 cm soil sensor) and **R = 0.98** (at 20 cm depth). More importantly, the data pairs are distributed along the first median, indicating that within the observation period (April–October) temperatures increased at nearly identical rates, even though soil temperatures were generally lower than air temperatures except towards the end of the analysis period.

- **Results of the Maixner and Johannesen (2014) Model for the Investigated Sites and Years**

Urtica dioica: Of the 22 weather stations available from the ClimVino project, the seven closest to the sampling sites were selected. Based on the local climatic conditions, the timing of *H. obsoletus* adult emergence (flight onset) was estimated using the Maixner and Johannesen (2014) model (**Table 3**).

Table 3. Predicted flight onset of *H. obsoletus* according to data from the seven relevant weather stations for the years 2023–2025. A: predicted flight onset per weather station; B: mean temporal distance of predicted onset dates between investigation years.

© 2025 by the author(s). Distributed under a Creative Commons CC BY license.

Preprints.org (www.preprints.org) | NOT PEER-REVIEWED | Posted: 6 November 2025 doi:10.20944/preprints202510.2130.v1

A

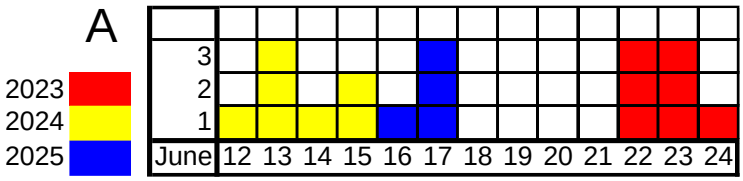

B

	2023	2024	2025
2023	0	8,8	5,75
2024		0	3,5
2025			0

In **2024**, the predicted flight onset of *H. obsoletus* is comparatively early—between **12 and 15 June**, depending on the weather station—and shows relatively high variability. In **2025**, emergence is slightly later (**16–17 June**) and less variable, partly due to data exclusion from three stations where temperature sensors temporarily failed. In contrast, **2023** shows a later predicted flight onset (**22–24 June**).

The mean temporal difference between flight onset across years is greatest between **2023 and 2024** (almost nine days) and smallest between **2024 and 2025** (approximately three and a half days). The variation between sites within a single year is too small to meaningfully compare with the host plant phenological data, whereas interannual differences are sufficient to allow such comparison.

Convolvulus arvensis: For *C. arvensis*, the weather stations correspond to the phenology sampling sites (with the exception of Donnerskirchen–Goldberg). As in *U. dioica*, differences in the predicted flight onset of *H. obsoletus* within a given year are minor, but interannual variation is more pronounced—especially between **2024 and 2025**. The predicted onset dates are generally earlier than those for *U. dioica*:

- **2024:** between **25 and 28 May** (Donnerskirchen–Wolfsbrunnbach slightly later),
- **2025:** between **2 and 4 June**,
- **2023:** between **8 and 10 June**.

The temporal shift between **2024 and 2025** is notably greater than in *U. dioica*—on average **7.5 days** versus **3.5 days**—while the interval between **2023 and 2024** is almost **13 days**. Only the difference between **2023 and 2025** is roughly comparable for both host species (**Table 4**).

Table 4. Predicted flight onset of *H. obsoletus* based on temperature data from the five *C. arvensis* sampling sites between 2023 and 2025 (A). B: Mean temporal difference in predicted flight onset between investigation years for each site.

A

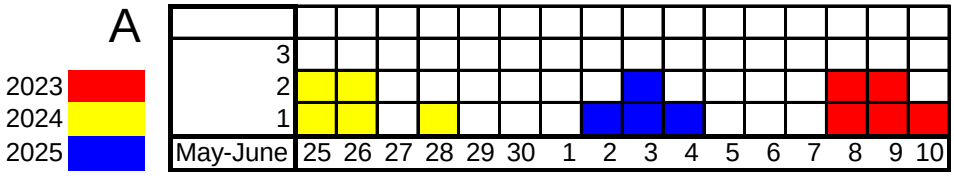

B

	2023	2024	2025
2023	0	12,75	5,5
2024		0	7,5
2025			0

- **Phenology of *Urtica dioica* from 2023 to 2025**

Vegetative development: During the observation period (from the fourth week of February, i.e. calendar week 10, to the second week of June, calendar week 24), **stem length** increased almost

© 2025 by the author(s). Distributed under a Creative Commons CC BY license.

Preprints.org (www.preprints.org) | NOT PEER-REVIEWED | Posted: 6 November 2025 doi:10.20944/preprints202510.2130.v1

exponentially, accompanied by a steady rise in variance. In total, **743 stems** were measured. The best-fitting linearised model describing the temporal pattern was

$Y = (a + bX^2)^2$, where Y denotes stem length and X the day of the year (DOY), while a and b are constants. (Statgraphics XV provides 27 potential models and ranks them according to goodness of fit.) The coefficient of determination was **R = 0.89.**

Growth commenced in **calendar week 10 (2023)**, slightly later in **2024**, and considerably later in **2025**, beginning in the **second week of March**. However, by June the differences had nearly levelled out. By this time, stems frequently exceeded **1 m in length**, though variability remained high. Ultimately, no significant differences between years could be observed (Figure 12).

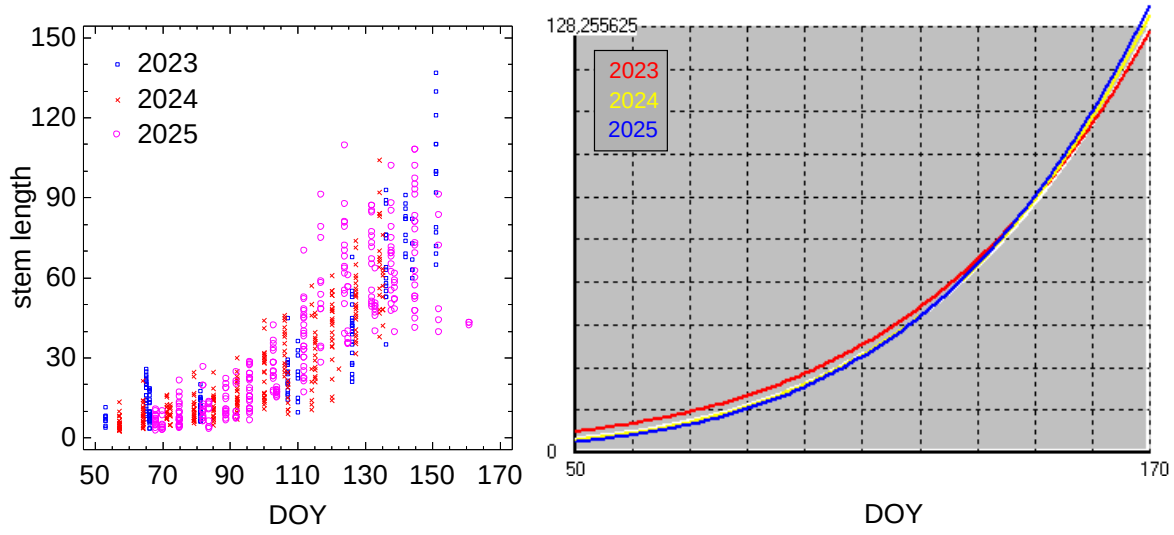

Figure 12. Change in stem length over the observation period (approximately DOY 50 = calendar week 8 to DOY 160 = calendar week 24) for the three study years. DOY = day of year. Left: raw data; right: regression curves.

With increasing stem length, the **number of** internodes also rose, albeit to a much lesser degree. Consequently, the slope of the best-fitting model—again **$Y = (a + bX^2)^2$**—was less pronounced, and the fit poorer (**R = 0.71**).

At the beginning of the season, stems typically bore about **five internodes**, increasing to around **15** by the end. In **2023**, the rate of increase was slightly lower than in the other years, which caused the extrapolated model to predict fewer internodes by the end of the observation period—an artefact not fully supported by the data, since internode numbers plateaued towards the end. **727 stems** were analysed.

© 2025 by the author(s). Distributed under a Creative Commons CC BY license.

Preprints.org (www.preprints.org) | NOT PEER-REVIEWED | Posted: 6 November 2025 doi:10.20944/preprints202510.2130.v1

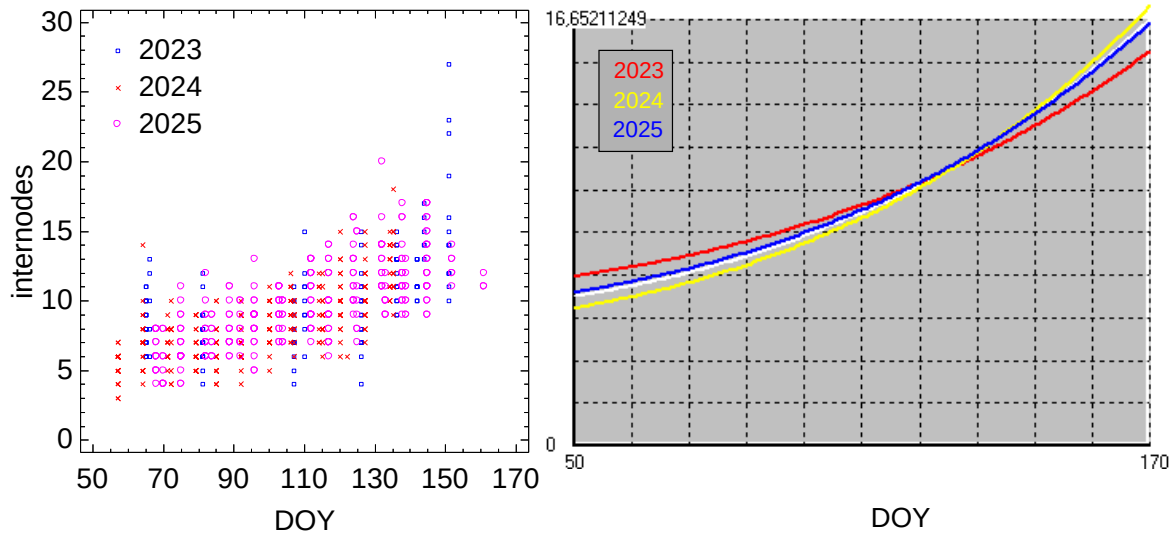

Figure 13. Change in number of internodes over the observation period. Left: raw data; right: regression curves.

The number of leaves per stem can at most equal twice the number of internodes, but was often lower—especially toward the end of the period. Initially, stems carried around **ten leaves**, later **20–25** on average.

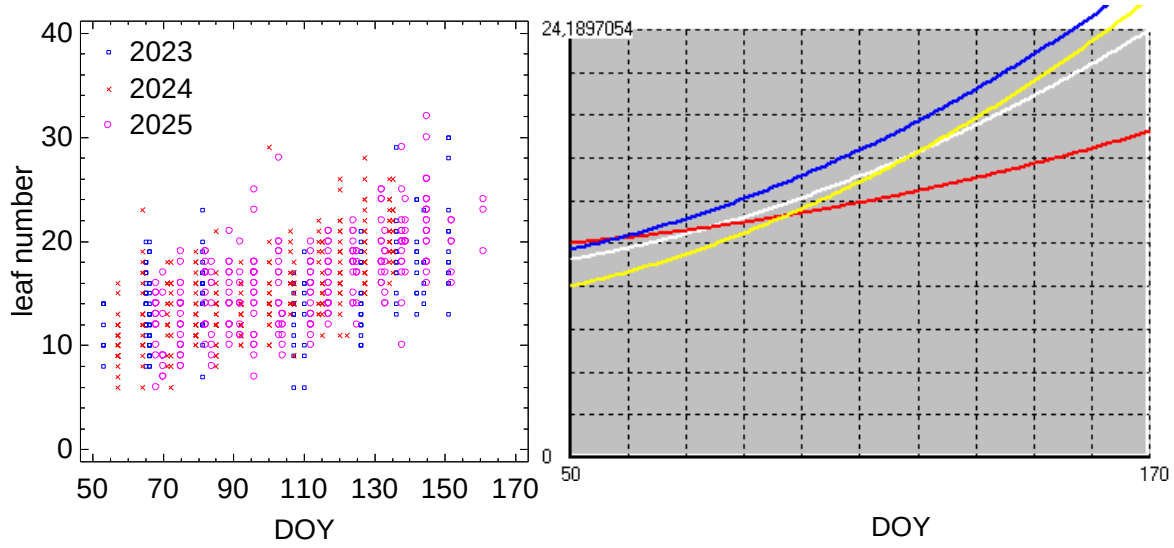

Figure 14. Change in number of leaves per stem over the observation period. Left: raw data; right: regression curves.

The 2023. than in the comparison years, resulting in a lower predicted leaf number by early June. However, the overall model fit was weak (**R = 0.6**). Leaf counts were recorded for **757 stems**.

The area per leaf changed substantially during the study, from a few cm² early in the season to **60 cm² or more** by early June. Considerable variability was observed depending on leaf position along the stem. The best-fitting linearised model was $\mathbf{Y = aX^b}$, with a correlation coefficient of **R = 0.77**.

The rate of increase was greater in **2025** than in the other years, primarily because growth began later. The power function tended to overestimate leaf area toward the end of the period, as growth had already plateaued.

© 2025 by the author(s). Distributed under a Creative Commons CC BY license.

Preprints.org (www.preprints.org) | NOT PEER-REVIEWED | Posted: 6 November 2025 doi:10.20944/preprints202510.2130.v1

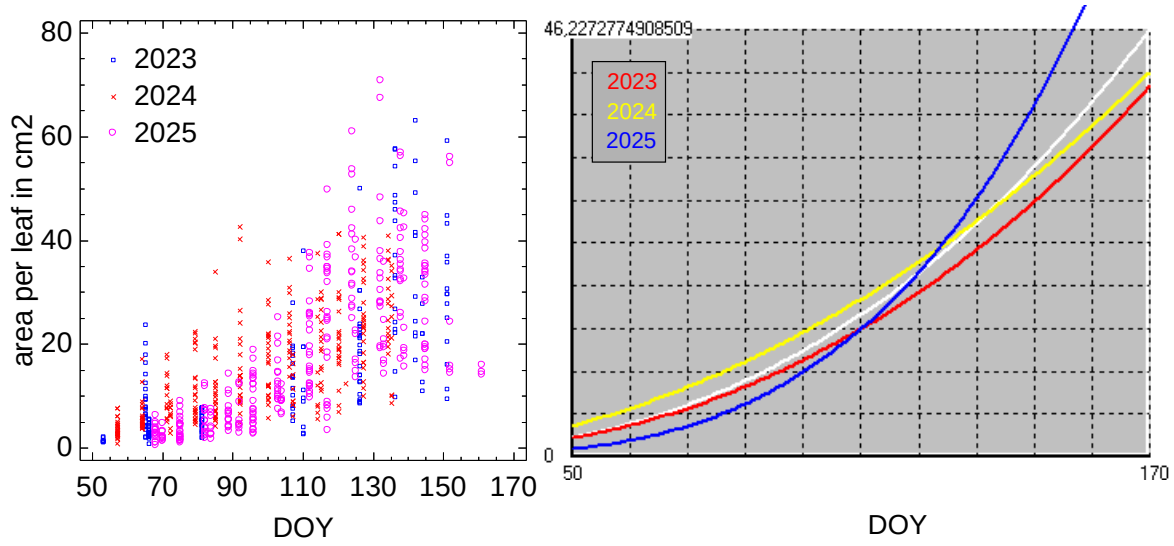

Figure 15. Change in area per leaf over the observation period. Left: raw data; right: regression curves.

The total leaf area per stem, derived from the product of leaf area and leaf number, could exceed **1,500 cm²** by the end of the observation period (Figure 16). This variable combines interannual differences between both contributing factors, which results in more pronounced variation in the regression curves: the largest total leaf area occurred in **2025**, followed by **2024** and **2023**. However, variability was so high that total leaf area proved unsuitable for illustrating interannual differences in vegetative phenology.

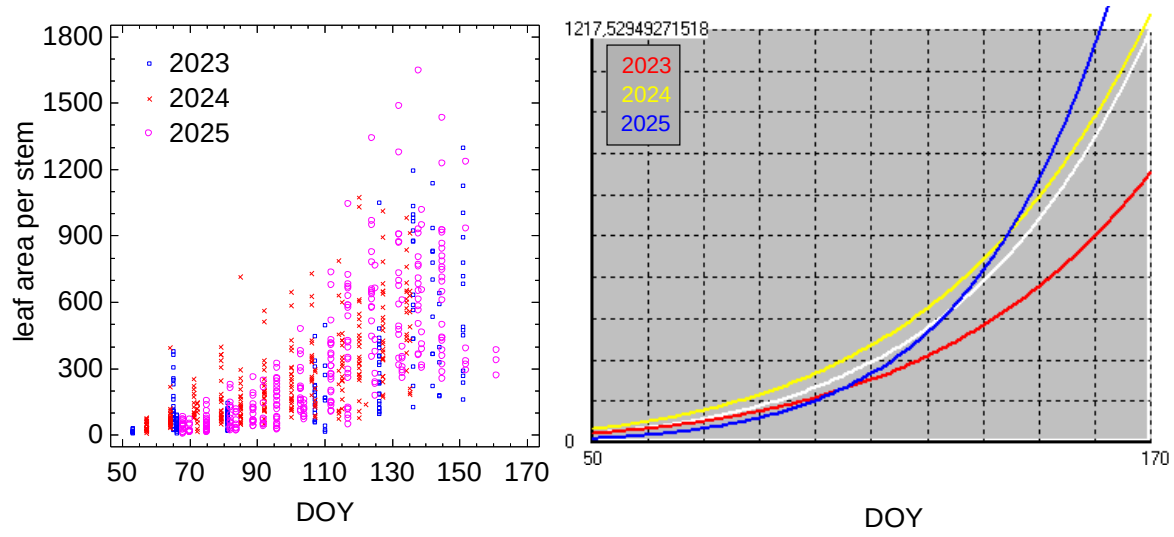

Figure 16. Change in total leaf area per stem over the observation period. Left: raw data; right: regression curves.

In summary, **vegetative development** towards the end of the observation period did not clearly reflect interannual climatic differences.

Generative development: The situation was different for **generative development (Figure 17).** For each site and sampling date, the **median flower developmental stage** (as defined in the Methods section) was determined separately for male and female inflorescences. In addition, **the number of distal nodes bearing inflorescences** was recorded at each site and time point.

Among **female flowers**, a **median stage of one or higher** within inflorescences was first reached in:

© 2025 by the author(s). Distributed under a Creative Commons CC BY license.

Preprints.org (www.preprints.org) | NOT PEER-REVIEWED | Posted: 6 November 2025 doi:10.20944/preprints202510.2130.v1

- **2024:** the penultimate week of May,
- **2025:** the first week of June, and
- **2023:** the second week of June.

This order mirrors the cumulative temperature sums for each year and thus corresponds well to the **predicted flight onset of** *H. obsoletus* according to Maixner and Johannesen (2014), bearing in mind that approximately **two weeks** typically elapse between reaching the first flower stage and adult emergence.

A similar pattern was observed when determining the time at which more than four inflorescence-bearing nodes first appeared:

- **2024:** penultimate week of May,
- **2025:** first week of June,
- **2023:** second week of June.

For **male flowers**, the situation differed slightly. When using the criterion of inflorescences with a **median stage ≥ 2**, this threshold was reached in:

- **2024:** penultimate week of May,
- **2025:** last week of May, and
- **2023:** second week of June.

This timing aligns well with the *H. obsoletus* flight predictions, apart from a consistent offset of about two weeks.

In terms of the **number of inflorescence-bearing nodes**, five or more were reached in:

- **2024 and 2025:** simultaneously (penultimate week of May),
- **2023**: this stage occurred much later—in the **second week of June**.

© 2025 by the author(s). Distributed under a Creative Commons CC BY license.

Preprints.org (www.preprints.org) | NOT PEER-REVIEWED | Posted: 6 November 2025 doi:10.20944/preprints202510.2130.v1

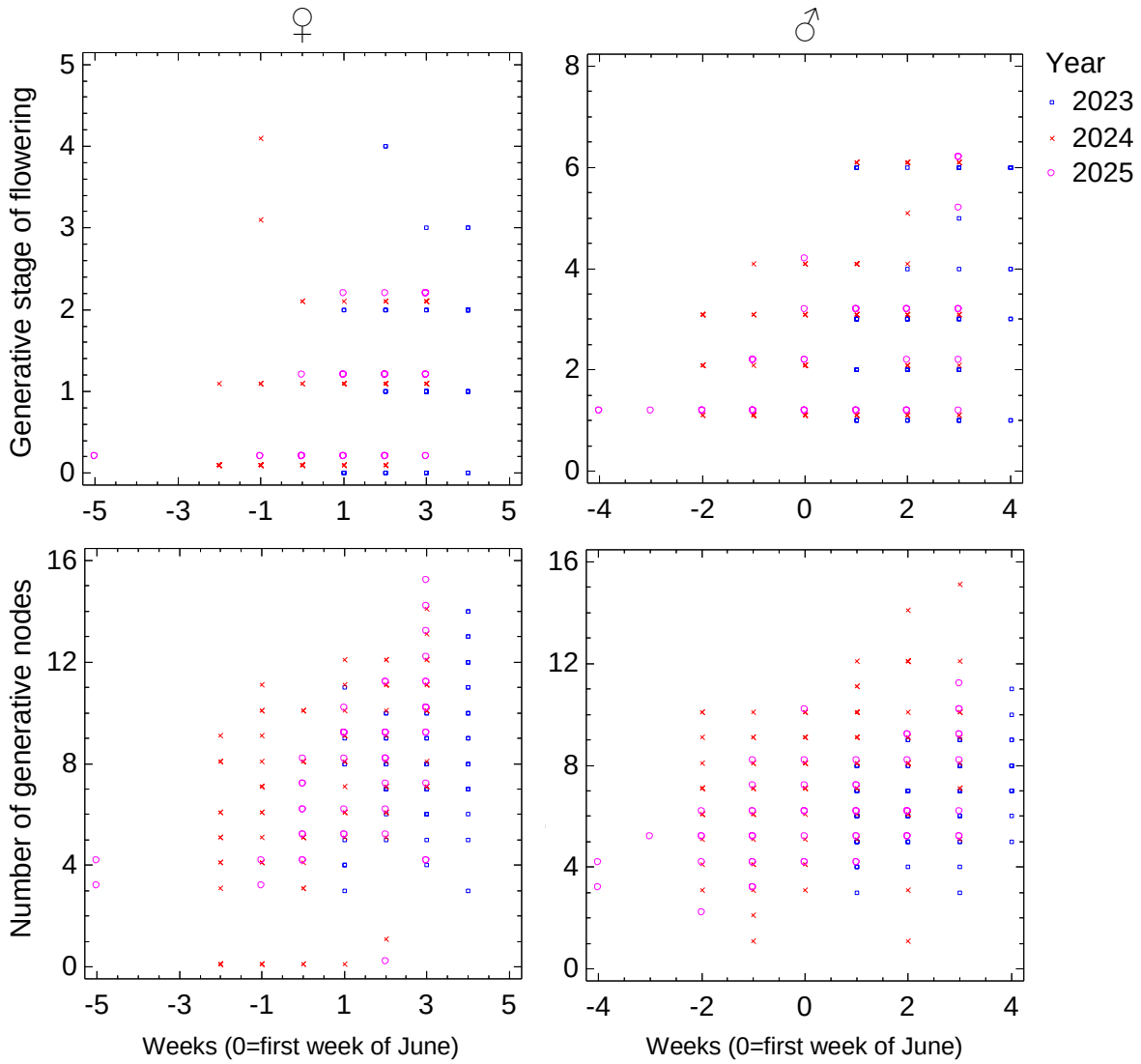

Figure 17. Median flower developmental stage (top) and number of distal nodes with inflorescences (bottom) in *U. dioica* stems, separated by sex.

In summary, **generative development**, in contrast to vegetative growth, provides a clear indication of interannual variation. For comparison with the **predicted or observed flight onset of** *H. obsoletus*, the **number of generative nodes bearing female flowers** appears to be the most suitable indicator, given its simplicity and applicability to large numbers of *U. dioica* stems.

- **Phenology of *Convolvulus arvensis* from 2023 to 2025**

Vegetative development: The above-ground development of *C. arvensis* begins considerably later than that of *U. dioica*, and the onset varied between the study years.

In **2024**, the first shoots appeared around **DOY 100** (early in the second week of April), in **2025** towards the **end of the third week of April (DOY 110)**, and in **2023** only in the **fourth week (DOY 116)**. The development of **shoot length, internode number, leaf number**, and **leaf area** was more linear than in *U. dioica*.

Nevertheless, a **power function ($Y = a + X^b$)** best described the temporal change in **main shoot length**, with a **moderate fit (R = 0.66)** based on measurements from **410 shoots**. In a linear model, the negative intercept was smallest for **2023** (indicating the latest onset of growth), followed by **2025** and **2024**. Conversely, the slope decreased in the same order. This can be interpreted as indicating that the later development begins, the faster it progresses thereafter. Consequently, by early June, no substantial differences in vegetative development remained between years. By then, main shoots

© 2025 by the author(s). Distributed under a Creative Commons CC BY license.

Preprints.org (www.preprints.org) | NOT PEER-REVIEWED | Posted: 6 November 2025 doi:10.20944/preprints202510.2130.v1

frequently exceeded **80 cm**, with considerable variance (Figure 18). Lateral shoots were not considered in this analysis.

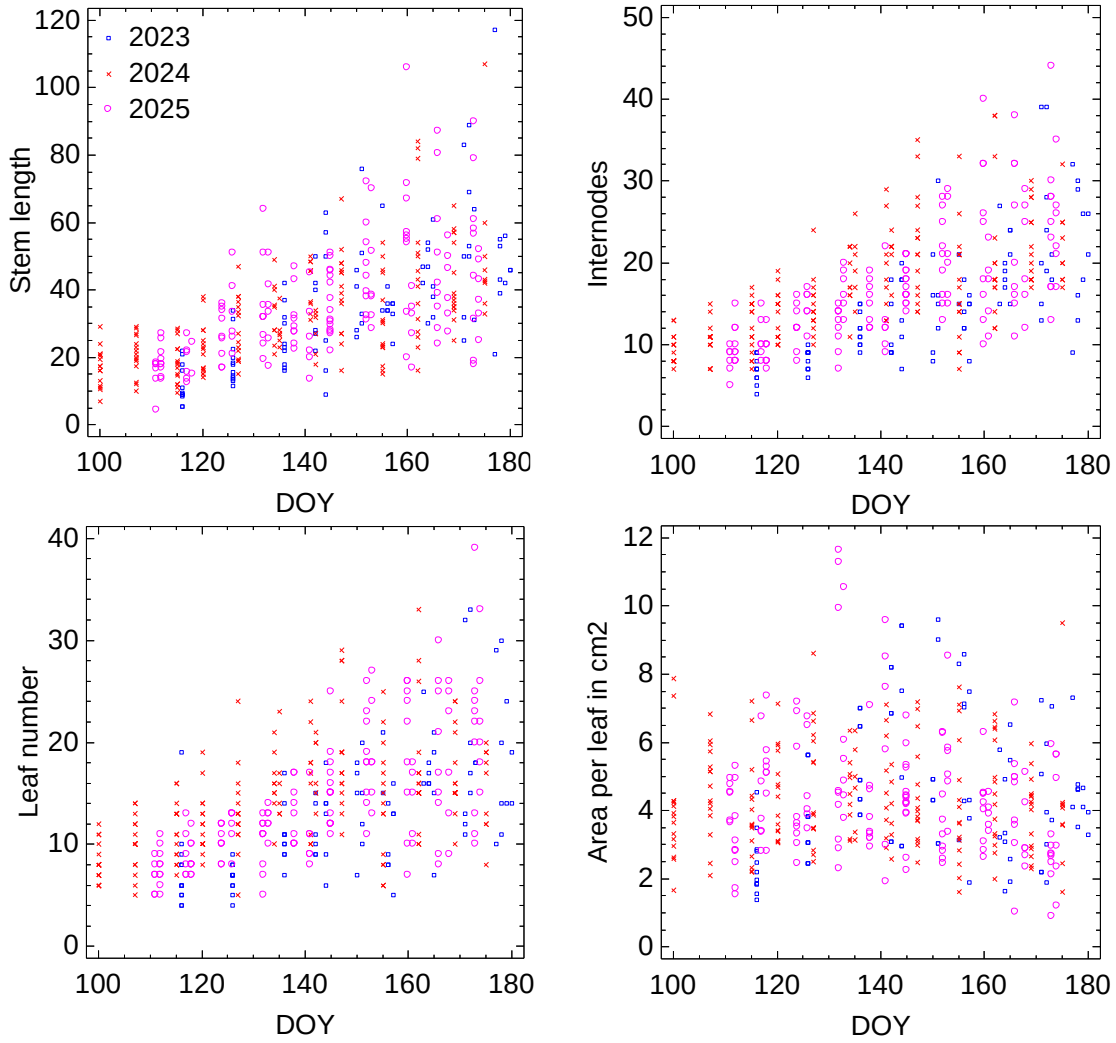

Figure 18. Change in selected vegetative traits of *C. arvensis* during spring (2023–2025).

The **temporal change in** internode number was also best described by a power function among all tested models that can be linearised (**R = 0.66**, n = 416). The relationship between intercept and slope among years mirrored that of main shoot length. However, the rate of increase for internode number was distinctly lower than that for shoot length, meaning that internodes elongated progressively through spring. Their number rose from approximately **10 in April** to **30 or more in June (**Figure 18**)**.

The **development of** leaf number followed a similar trend, although the loss of basal leaves meant this relationship was not fully consistent. Despite such losses, main shoots often carried about **30 leaves in June**, compared to **around ten in April**, again with high variance. The best-fitting linearised model was a power function with a poorer fit (**R = 0.58**, n = 416). Regression lines for **2023** and **2025** were nearly identical, while **2024** showed a noticeably higher intercept and a slope approximately half that of the other two. By late May and early June, the initial annual differences had nearly evened out.

None of these vegetative traits were suitable for analysing the influence of climatic variation on phenological development.

© 2025 by the author(s). Distributed under a Creative Commons CC BY license.

Preprints.org (www.preprints.org) | NOT PEER-REVIEWED | Posted: 6 November 2025 doi:10.20944/preprints202510.2130.v1

In contrast to *U. dioica*, the area of one leaf (**mean** per shoot) of *C. arvensis* showed virtually **no seasonal change**. However, substantial differences occurred **between sites**. With a sample size of **416**, neither a power function nor a linear model adequately represented temporal variation; in the linear model, the correlation coefficient was **near zero**, and the slopes for all three years were also close to zero, confirming that leaf area remained effectively constant. No significant differences between years were found (**ANOVA, p = 0.75**).

Generative development: In **2023**, the first **closed and open flowers** were observed on **6 June** at the site Winden am See. During the same week, flowering began in **Donnerskirchen** (both vineyards), followed one week later by **Großhöflein** and **Gols**. Generative buds had appeared approximately **one week earlier** in all cases.

In **2024**, the first open flowers were recorded on **27 May** at **Donnerskirchen–Wolfsbrunnbach**, with generative buds already present one week before. In the following week, flowering began at **Donnerskirchen–Goldberg** and **Großhöflein**, where buds had been visible by **mid-May**.

By **10 June 2025**, **closed and open flowers** were recorded at all sites, though observations of flowering outside the sampling locations dated back to **22 May**. On **2–3 June**, flower buds were visible at all sites except **Donnerskirchen–Wolfsbrunnbach**.

A correspondence between **flowering onset** and the **flight onset predictions** based on the **Maixner and Johannesen (2014)** model could be observed for **2024**. In **2023** and **2025**, flowering occurred later, consistent with the later predicted emergence of *H. obsoletus*. However, flowering in **2025** began only slightly earlier than in **2023**, i.e. still later than the predicted flight onset. One limitation is the relatively high **heterogeneity in flowering onset among sites**, which does not perfectly reflect local weather patterns and likely depends on additional local factors.

The present investigations were based on the **hypothesis** that the **below-ground larval development** of *H. obsoletus* is critically influenced by **host phenology**, in that the **ectoparasitic insect** exploits **physiological signals of its host plant** to regulate its own development. This hypothesis can only be conclusively tested under controlled laboratory conditions, for which the necessary resources were not available. Consequently, we addressed two related questions:

1. **What physical cues regarding seasonal periodicity are available to an organism living at depths of about 5–20 cm?**
2. **If the above hypothesis is correct, how can host physiology be utilised to improve models predicting the timing of adult emergence in** *H. obsoletus***?**

Since larvae living in the soil cannot directly perceive photoperiodic changes, only **daily temperature fluctuations** remain as a possible indirect indicator of day length. Through **simulations** and **analysis of soil temperature sensors**, we demonstrated that the **temperature amplitude at 20 cm depth** constitutes only **9–17%** of that at the soil surface. On days with minimal diurnal variation, this may provide insufficient information, implying that **non-physical cues** must be used to achieve synchronised emergence. Interestingly, there are **soil-dwelling planthoppers** such as *Pentastiridius leporinus* that overwinter in highly variable developmental stages but still undergo adult emergence relatively synchronously in late spring.

Regarding the second question, we examined whether vegetative or generative development of the host plants could improve the accuracy of flight-onset models for *H. obsoletus*, assuming that the timing of adult emergence is causally linked to host phenology. For the vegetative parameters analysed—stem or shoot length, number of internodes, leaf number, and leaf area—this was not the case. Variability and measurement effort were too high. Variance might be reduced by selectively sampling the most advanced individuals rather than random ones. In *C. arvensis*, leaf area remained constant throughout the season and was therefore entirely unsuitable. The growth rates (weekly change) of other parameters were too dependent on short-term weather conditions to serve as reliable indicators.

By contrast, the generative development proved more suitable. Although individual inflorescences of *U. dioica* contained flowers at varying stages, the number of inflorescence-bearing nodes was easy to determine and exhibited temporal correspondence with the predicted flight onset.

© 2025 by the author(s). Distributed under a Creative Commons CC BY license.

Preprints.org (www.preprints.org) | NOT PEER-REVIEWED | Posted: 6 November 2025 doi:10.20944/preprints202510.2130.v1

However, male and female plants must be analysed separately. Based on current data, a corresponding correlation for *C. arvensis* flowering onset cannot be ruled out, even though local variability exists that cannot be explained solely by temperature accumulation.

Acknowledgments: Funding for the IoT weather sensors and access to the corresponding data were provided within the framework of the StolReg project ("Control of Stolbur Phytoplasma pathogens in potato, vegetable, sugar beet and viticulture", 01.10.2021–30.09.2022). Special thanks are due to M. Riedle-Bauer and G. Brader.

References

1. Alexander R.D., Moore T.E., The evolutionary relationships of 17-year and 13-year cicadas, and three new species (Homoptera, Cicadidae, Magicicada). Misc. Publ, Mus. Zool. Univ.
2. Mich. 121, 1-59, 1962.
3. Aryan, A., Brader, G., Mörtel, J., Pastar, M., and Riedle-Bauer, M., An abundant 'Candidatus Phytoplasma solani' tuf b strain is associated with grapevine, stinging nettle, and H*yalesthes obsoletus*. Eur. J. Plant Pathol. 140, 213–227, 2014. doi: 10.1007/s10658-014-0455-0
4. Fourier, J., Théorie analytique de la chaleur, Paris 1822.
5. Imo, M., Maixner, M., and Johannesen, J., Sympatric diversification vs. immigration: deciphering host-plant specialization in a polyphagous insect, the stolbur phytoplasma vector *Hyalesthes obsoletus* (Cixiidae). Mol. Ecol. 22, 2188–2203, 2013.
6. doi: 10.1111/mec.12237.
7. Johannesen, J., and Riedle-Bauer, M., Origin of a sudden mass occurrence of the stolbur phytoplasma vector *Hyalesthes obsoletus* (Cixiidae) in Austria. Ann. Appl. Biol. 165, 488–495, 2014. doi: 10.1111/aab.12158.
8. Jovic, J., Riedle-Bauer, M., and Chuche, J., "Vector role of cixiids and other planthopper species," in Plant Pathogenic Bacteria - II, eds A. Bertaccini, P. Weintraub, G. Rao, and N. Mori (Singapore: Springer), 79–113, 2019. doi: 10.1007/978-981-13-2832-9_4.
9. Karban, R. Black, C.A., Weinbaum, S.A., How 17-year cicadas keep track of time, Ecology Letters 3(4), 253-256, 2000.
10. Landi, L., Riolo, P., Murolo, S., Romanazzi, G., Nardi, S., and Isidoro, N., Genetic variability of stolbur phytoplasma in *Hyalesthes obsoletus* (Hemiptera: Cixiidae) and its main host plants in vineyard agroecosystems. J. Econ. Entomol. 108, 1506–1515, 2015.
11. doi: 10.1093/jee/tov103
12. Langer, M., and Maixner, M., Molecular characterisation of grapevine yellows associated phytoplasmas of the stolbur-group based on RFLP-analysis of non-ribosomal DNA. Vitis 43, 191–199, 2004. doi: 10.5073/vitis.2004.43.191-199
13. Maixner, M., Langer, M., Prediction of the flight of *Hyalesthes obsoletus*, vector of stolbur phytoplasma, using temperature sums, IOBC WPRS Bulletin 29(11), 161-166, 2004.
14. Maixner, M., Johannesen, J., Optimized monitoring of host populations of the Bois noir vector, Hyalesthes obsoletus, based on flight phenology observations. Working Group "Integrated protection and production in Viticulture": Proceedings of the meeting at Ascona (Switzerland), 13th – 17th October, 2013, IOBC WPRS Bulletin = Bulletin OILB SROP, 105, 151-157, 2014.
15. Mori, N., Cargnus, E., Martini, M., Pavan, F., Relationships between *Hyalesthes obsoletus*, Its Herbaceous Hosts and Bois Noir Epidemiology in Northern Italian Vineyards. Insects 11, 606, 2020. https://doi.org/10.3390/insects11090606
16. Panassiti B, Breuer M, Marquardt S, Biedermann R. Influence of environment and climate on occurrence of the cixiid planthopper *Hyalesthes obsoletus*, the vector of the grapevine disease 'bois noir'. Bull Entomol Res. 2013 Dec;103(6):621-33. doi: 10.1017/S0007485313000163. Epub 2013 Apr 29. PMID: 23628148.
17. Paulauskienė, A.; Tarasevičienė, Ž.; Laukagalis, V. Influence of Harvesting Time on the Chemical Composition of Wild Stinging Nettle (*Urtica dioica* L.). Plants 2021, 10, 686. https://doi.org/10.3390/plants10040686

© 2025 by the author(s). Distributed under a Creative Commons CC BY license.

Preprints.org (www.preprints.org) | NOT PEER-REVIEWED | Posted: 6 November 2025 doi:10.20944/preprints202510.2130.v1

18. Quaglino, F., Zhao, Y., Casati, P., Bulgari, D., Bianco, P. A., Wei, W., et al., 'Candidatus Phytoplasma solani', a novel taxon associated with stolbur- and bois noir-related diseases of plants. Int. J. Syst. Evol. Microbiol. 63, 2879–2894, 2013. doi: 10.1099/ijs.0.044750-0
19. Riedle-Bauer, M., Mörtel, M., Pastar, M., Aryan, A., & Brader, G. (2013). Mass occurence of *Hyalesthes obsoletus* on *Urtica dioica* in Austria and sole presence of tuf-type b stolbur phytoplasma on stinging nettles, grapevine and the transmitting insects. In Proceedings of the 3rd European Bois Noir Workshop (pp. 26-27)
20. Sforza, R., Bourgoin, T., Wilson, S.W., Boudon-Padieu, E., Field observations, laboratory rearing and description of immatures of the planthopper *Hyalesthes obsoletus* (Hemiptera: Cixiidae), Eur. J. Entomol 96, 409-418, 1999.
21. Šrůtek M. & Teckelmann M. (1998) Review of biology and ecology of *Urtica dioica*. – Preslia 70: 1–19
22. Tiefenbrunner, A.; Tiefenbrunner, W. Contributions to the Description of the Instars of the Planthopper *Hyalesthes obsoletus* (Fulgoromorpha, Hemiptera). Preprints 2025, 2025020848. https://doi.org/10.20944/preprints202502.0848.v1

Disclaimer/Publisher's Note: The statements, opinions and data contained in all publications are solely those of the individual author(s) and contributor(s) and not of MDPI and/or the editor(s). MDPI and/or the editor(s) disclaim responsibility for any injury to people or property resulting from any ideas, methods, instructions or products referred to in the content.

© 2025 by the author(s). Distributed under a Creative Commons CC BY license.